Segmentation-Based MR Attenuation Correction Including Bones Also Affects Quantitation in Brain Studies: An Initial Result of ^{18}F-FP-CIT PET/MR for Patients with Parkinsonism

Hongyoon Choi[1,2], Gi Jeong Cheon[1,3], Han-Joon Kim[4], Seung Hong Choi[5,6], Jae Sung Lee[1], Yong-il Kim[1,2], Keon Wook Kang[1,3], June-Key Chung[1,3], E. Edmund Kim[2,7], and Dong Soo Lee[1,2]

[1]Department of Nuclear Medicine, Seoul National University Hospital, Seoul, Korea; [2]Department of Molecular Medicine and Biopharmaceutical Science, Graduate School of Convergence Science and Technology, Seoul National University, Seoul, Korea; [3]Cancer Research Institute, Seoul National University, Seoul, Korea; [4]Department of Neurology, Seoul National University Hospital, Seoul, Korea; [5]Department of Radiology, Seoul National University College of Medicine, Seoul, Korea; [6]Center for Nanoparticle Research, Institute for Basic Science, and School of Chemical and Biological Engineering, Seoul National University, Seoul, Korea; and [7]Department of Radiological Sciences, University of California at Irvine, Irvine, California

Attenuation correction (AC) with an ultrashort echo time (UTE) sequence has recently been used in combination with segmentation for cortical bone identification for brain PET/MR studies. The purpose of this study was to evaluate the quantification of ^{18}F-fluoropropyl-carbomethoxyiodophenylnortropane (^{18}F-FP-CIT) binding in brain PET/MR, particularly focusing on effects of UTE-based AC including bone segmentation. **Methods:** Sixteen patients with initially suspected parkinsonism were prospectively enrolled. An emission scan was acquired 110 min after ^{18}F-FP-CIT injection on a dedicated PET/MR scanner, immediately followed by another emission scan using a PET/CT scanner 120 min after the injection. A UTE-based attenuation map was used to classify the voxels into 3 tissues: bone, soft tissue, and air. All PET images were spatially normalized, and a specific-to-nonspecific dopamine transporter (DAT) binding ratio (BR) was calculated using statistical probabilistic anatomic mapping. The level of agreement was assessed with intraclass correlation coefficients (ICCs). Voxelwise comparison between PET images acquired from PET/MR and PET/CT was performed. We compared non–attenuation-corrected images to analyze UTE-based AC effects on DAT quantification. **Results:** BR in the putamen obtained from PET/MR and PET/CT showed low interequipment variability, whereas BR in the caudate nucleus showed significant variability (ICC = 0.967 and 0.682 for putamen and caudate nucleus, respectively). BR in the caudate nucleus was significantly underestimated by PET/MR, compared with PET/CT (mean difference of BR = 0.66, $P < 0.0001$). Voxelwise analysis revealed that PET/MR showed significantly low BR in the periventricular regions, which was caused by a misclassification of the ventricle as air on the attenuation map. We also compared non-AC images, revealing low interequipment variability even in the caudate nucleus (ICC = 0.937 and 0.832 for putamen and caudate nucleus, respectively). **Conclusion:** Our data demonstrate spatial bias of the DAT BR on ^{18}F-FP-CIT PET/MR. Voxelwise analysis and comparison to non-AC images identified the misclassification of ventricle as air to be the cause of bias. To obtain reliable quantification for brain PET/MR studies including ^{18}F-FP-CIT PET, alternative and more reliable segmentation strategies are required.

Key Words: PET/MR; ^{18}F-FP-CIT; UTE sequence; attenuation correction; brain PET

J Nucl Med 2014; 55:1617–1622
DOI: 10.2967/jnumed.114.138636

CT images from hybrid devices such as a PET/CT scanner have been used for γ-ray attenuation correction (AC) and anatomic localization (*1,2*). However, CT images have limitations in PET quantification in the brain structures due to the lack of soft-tissue differentiation. In brain PET imaging, ^{18}F-fluoropropyl-carbomethoxyiodophenylnortropane (^{18}F-FP-CIT) has been widely used for evaluation of Parkinsonian syndrome as dopaminergic system imaging (*3,4*). For quantification of dopamine transporter (DAT) density, manually drawn regions of interest or software-based coregistered additional MR images have been used to overcome the issues regarding striatal segmentation (*5–7*). However, previously used coregistration methods could be inaccurate, particularly in the case of DAT images because of the possibility of misregistration between the 2 different images (*8,9*).

Currently, hybrid PET/MR systems are being used in clinical studies. Simultaneous acquisition of PET and MR images can solve the above issues regarding brain structure definition and coregistration. Before making use of simultaneously acquired MR for anatomically accurate PET quantification, routinely acquired brain PET/MR should be proved to be equivalent to previous PET/CT scanners.

In PET/MR systems, one of the difficulties to be adopted in clinical routine is MR-based AC (*10*). Various techniques have been suggested to derive an attenuation map (*11*). Commercial PET/MR systems today use segmentation-based AC based on an attenuation map derived from MR images. They separate MR images into 3 tissue segments (soft tissue, lung, and air) (*12*) or 4 tissue segments (water, fat, lung, and air) (*13*). However, bone segmentation using MR is not routinely performed in commercial PET/MR systems because it is

Received Feb. 7, 2014; revision accepted Jul. 21, 2014.
For correspondence or reprints contact either of the following:
Gi Jeong Cheon, Department of Nuclear Medicine, Seoul National University College of Medicine, 101 Daehangro, Jongro-gu, Seoul 110-744, Korea.
E-mail: larrycheon@gmail.com
Han-Joon Kim, Department of Neurology, Seoul National University College of Medicine, 101 Daehangro, Jongro-gu, Seoul 110-744, Korea.
E-mail: movement@snu.ac.kr
Published online Aug. 11, 2014.

hard to distinguish bone with standard pulse sequences (*10*), even though ignoring bone for AC significantly affects PET activity quantification (*14–16*).

Recently, a new method has been introduced to distinguish bone using an ultrashort echo time (UTE) sequence (*17,18*). When a UTE sequence is used, cortical bone structures can be distinguished by short relaxation time. UTE sequences have been applied to segmentation-based AC including bone to reduce the bone attenuation–related bias. However, previous studies revealed that UTE-based AC had errors in determining a boundary between soft tissue and air (*18,19*). Thus, bone segmentation in PET/MR systems remains an important issue, and several protocols and algorithms have been developed.

For quantitative analysis, static PET images can be used when ^{18}F-FP-CIT reaches equilibrium binding in the brain, because a simple ratio of regional counts is proportional to binding potential (*20,21*). However, it remains unclear whether quantitative ^{18}F-FP-CIT binding potential acquired from PET/MR is concordant with that from PET/CT because of the differences in AC methods and hardware. As we previously discussed, to maximize advantages of simultaneously acquired MR in PET/MR scanners, an agreement between PET/MR and PET/CT in quantification should be first tested.

The purpose of our study was to assess the quantification of ^{18}F-FP-CIT binding using PET/MR, compared with PET/CT. We applied UTE-based segmentation to obtain attenuation maps to minimize the effects of neglecting bone. Interequipment agreement between PET/MR and PET/CT was assessed on prospectively enrolled patient data, and we analyzed quantification bias of ^{18}F-FP-CIT PET/MR with regard to UTE-based AC.

MATERIALS AND METHODS

Patients

Sixteen patients (8 men, 8 women; mean age, 61.3 y; age range, 39–77 y) with initially suspected Parkinson disease were prospectively enrolled. This study was approved by the Institutional Review Board of our institute. All study participants signed an informed consent form.

The following were inclusion criteria: subjects were older than 20 y and were clinically suspected of having parkinsonism due to tremor, rigidity, or hypokinesia.

PET/CT and PET/MR Acquisition

Patients underwent PET/CT and PET/MR after an injection of 185 MBq (5 mCi) of ^{18}F-FP-CIT. Emission scans were acquired 110 min after injection using a PET/MR scanner (Biograph mMR; Siemens Healthcare) for 10 min. Another emission scan was acquired using a PET/CT scanner (Biograph mCT; Siemens Healthcare), immediately after the first emission scan, followed by a CT scan for AC (mean start time difference between PET/MR and PET/CT, 14.3 min; range, 11.2–19.7 min).

PET images from the PET/CT and PET/MR were reconstructed using an iterative algorithm (ordered-subset expectation maximization). The reconstructed protocols were 24 subsets/5 iterations and 21 subsets/5 iterations on the PET/CT and PET/MR scanners, respectively, because numbers of 24 subsets were not available on our PET/MR system. The matrix size of all PET images was 256 × 256, and a 4-mm gaussian postreconstruction filter was applied.

MR imaging on our PET/MR system included a UTE sequence, performed with a repetition time of 11.9, echo time 1 (TE1) of 0.07, and echo time 2 (TE2) of 2.46 ms; flip angle of 10°; and 192 × 192 matrix size. The slice thickness was 1.6 mm, and field of view was 300 × 300 mm. AC maps were generated on the software incorporated into our PET/MR system using a segmentation-based approach. In brief, an R_2 map, the inverse of the T2 relaxation time, was used for distinguishing cortical bone and soft tissue. R_2 was calculated by 2 different echo times.

$$R_2 = \frac{lnI_1 - lnI_2}{\mathrm{TE2} - \mathrm{TE1}},$$

where I_1 and I_2 are the signal intensity at TE1 and TE2. To classify soft tissue and air density, a region-growing method was used. A mask of patients was derived to find the outer contour of patients using MR images with TE1. All voxels were classified into 3 tissues, including cortical bone, soft tissue, and air (*18*). The AC maps were generated by Biograph mMR software (version VB18P; Siemens) following the manufacturer's instructions. The maps used the predefined attenuation coefficient of each tissue (0.151 cm^{-1} for cortical bone, 0.100 cm^{-1} for soft tissue, and 0 cm^{-1} for air). Precomputed AC maps of local radiofrequency coils were used to minimize the hardware-related bias. Compared with the hardware components used for PET/CT acquisition, earplugs were additionally applied for PET/MR scans; however, they were not taken into account for further AC.

PET Image Analysis

We first performed visual analysis of ^{18}F-FP-CIT PET images. Two nuclear medicine physicians visually assessed DAT density in the striatum by consensus. We classified ^{18}F-FP-CIT PET scans into 2 groups: patients with or without nigrostriatal degeneration. PET scans acquired by PET/CT and PET/MR scanners were independently assessed and compared.

All the PET images were spatially normalized into an in-house ^{18}F-FP-CIT PET template (*5,22*). PET counts in the putamen, caudate nucleus, and cerebellum were calculated using statistical probabilistic anatomic mapping (*23*). We calculated the specific-to-nonspecific binding ratio (BR), defined as $BR = (C_{specific} - C_{nonspecific})/C_{nonspecific}$. PET counts of cerebellum were used as nonspecific counts, and BR of putamen ($BR_{putamen}$) and BR of caudate nucleus ($BR_{caudate}$) were calculated. We independently calculated the BR of bilateral striatum for each patient. The BR obtained from PET/CT and PET/MR was directly compared, and the level of agreement was assessed with intraclass correlation coefficients (ICCs). BR obtained from PET images before AC (non-AC PET) was calculated from PET/CT and PET/MR. Neither patients' attenuation factors nor hardware components were included for PET image reconstruction. BR calculated by the non-AC PET images was an inaccurate value for clinical purpose because quantification of ^{18}F-FP-CIT binding in deep gray matters is affected by attenuation. The purpose of BR obtained from non-AC images was to evaluate whether the difference between PET/CT and PET/MR was related to AC. The method for the image comparison analyses is summarized in Figure 1.

To evaluate spatial bias in PET/MR, a voxelwise analysis was also performed. Spatially normalized PET images from PET/CT and PET/MR were smoothed by a gaussian filter of 12 mm in full width at half maximum. PET counts in voxels were scaled into BR, and a paired *t* test was performed on a voxel basis between PET images from PET/CT and PET/MR. Image processing was performed using statistical parametric mapping (SPM5; University College of London). Uncorrected *P* values of less than 0.001 were set as the significance threshold, and an extent threshold of 100 contiguous voxels was applied. In addition, the difference between PET images from PET/CT and PET/MR was calculated on a voxel basis.

Statistics

Continuous variables are expressed as mean ± SD. ICCs and their 95% confidence intervals (CIs) were calculated to test the interequipment variability—that is, PET images from PET/CT and PET/MR

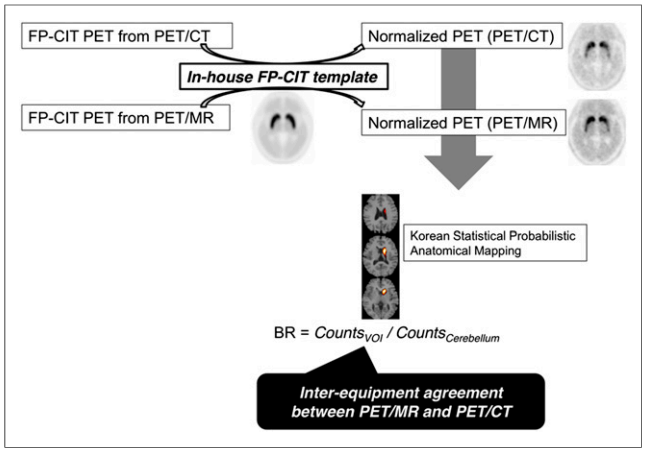

FIGURE 1. Schematic workflow for image processing and quantification. PET scans acquired from PET/MR and PET/CT were spatially normalized to Korean Statistical Probabilistic Anatomic Mapping template. BR was calculated using statistical probabilistic maps of putamen and caudate nucleus. Interequipment agreement between PET/MR and PET/CT was calculated. VOI = volume of interest.

(1-way random-effects model with absolute agreement). An ICC of 1 means perfect agreement, and an ICC greater than 0.8 is generally considered as excellent reliability (*24*). Bland–Altman plots were drawn to find interequipment variability. Statistical analyses were performed with MedCalc software (MedCalc 12).

RESULTS

Patients' Characteristics and Visual Assessment

Detailed information on all patients is shown in Table 1. According to the clinical features and physical examinations, the initial diagnosis of 14 patients was Parkinson disease and that of the other 2 patients was tremor not fulfilling the clinical diagnostic criteria for Parkinson disease. Twelve of the 14 patients with suspected Parkinson disease showed reduced DAT density on visual assessment. Two of them showed normal DAT density on visual assessment. The 2 patients with suspected non-Parkinsonian syndrome showed normal DAT density. The visual assessments of ^{18}F-FP-CIT PET/MR and PET/CT were performed, and patients were classified into the 2 groups: patients with decreased and preserved DAT density. The visual classification based on PET/CT was in agreement with that based on PET/MR.

Quantification of BR: Comparison of PET/CT and PET/MR

$BR_{putamen}$ calculated from PET/CT and PET/MR showed excellent interequipment agreement, whereas $BR_{caudate}$ showed comparable interequipment variability (ICC, 0.967; 95% CI, 0.841–0.989, and ICC, 0.682; 95% CI, −0.185–0.908 for putamen and caudate nucleus, respectively). The mean difference was 0.23 ± 0.28 for $BR_{putamen}$ and 0.66 ± 0.33 for $BR_{caudate}$. Figure 2 shows BR for all bilateral striata calculated from PET/CT and PET/MR. We constructed Bland–Altman plots to visually check the reliability between PET/CT and PET/MR (Figs. 2C and 2D). $BR_{putamen}$ and $BR_{caudate}$ showed narrow CIs; however, $BR_{caudate}$ on PET/MR was consistently lower than that on PET/CT.

We compared non-AC images from PET/CT and PET/MR to check whether UTE-based AC affected DAT BR quantification. Figure 3 shows BR for all bilateral striata calculated from non-AC images. $BR_{caudate}$ and $BR_{putamen}$ showed excellent interequipment reliability when non-AC images were used (ICC, 0.937; 95% CI, 0.873–0.969, and ICC, 0.832; 95% CI, 0.655–0.918 for putamen and caudate nucleus, respectively).

Voxelwise Analysis and Comparison of Attenuation Maps

To find the regions affected by UTE-based AC, voxelwise analysis was performed. A paired *t* test between PET images revealed that DAT BR in PET/MR was significantly lower in the periventricular area (Fig. 4). When UTE-based attenuation maps were used, significant portions of lateral ventricles were misclassified as air, causing underestimated BR in the periventricular area (Fig. 5). The misclassification of ventricles was consistently found in all the patients. The voxelwise difference map revealed underestimation

TABLE 1
Demographic Data of All Patients

Patient no.	Sex	Age (y)	Initial clinical assessment	Visual assessment of DAT density
1	M	56	Parkinson disease	Reduced in both striata
2	M	59	Parkinson disease	Reduced in both striata
3	F	71	Parkinson disease	Reduced in both striata
4	M	68	Parkinson disease	Reduced in both striata
5	F	50	Parkinson disease	Reduced in both striata
6	F	67	Nonparkinsonian tremor	Preserved in both striata
7	M	39	Parkinson disease	Reduced in both striata
8	F	68	Parkinson disease	Reduced in both striata
9	M	69	Parkinson disease	Preserved in both striata
10	F	64	Nonparkinsonian tremor	Preserved in both striata
11	M	54	Parkinson disease	Reduced in both striata
12	M	58	Parkinson disease	Reduced in both striata
13	M	54	Parkinson disease	Reduced in both striata
14	F	61	Parkinson disease	Reduced in both striata
15	F	65	Parkinson disease	Reduced in both striata
16	F	77	Parkinson disease	Preserved in both striata

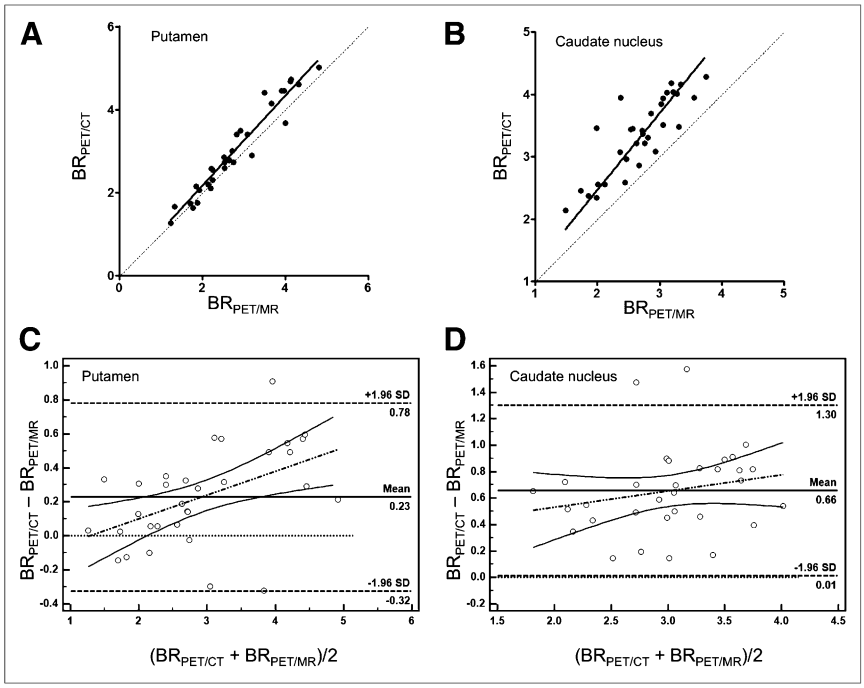

FIGURE 2. (A) DAT BR of PET/MR and PET/CT. BR of putamen calculated from PET/MR and PET/CT showed excellent interequipment agreement. ICC of BR was 0.967 (95% CI, 0.841–0.989). (B) BR of caudate nucleus calculated from PET/MR was underestimated, compared with PET/CT. ICC of BR was 0.682 (95% CI, −0.185–0.908). Bland–Altman plots show interequipment agreement in putamen (C) and caudate nucleus (D). Bland–Altman plot of caudate nucleus shows comparable variability between BR calculated from PET/MR and PET/CT, compared with putamen, which showed considerable mean difference of BR (0.23 ± 0.28 for putamen and 0.66 ± 0.33 for caudate nucleus).

in the periventricular area involving the caudate nucleus and lateral ventricles (Fig. 5D).

DISCUSSION

In this study, we identified a difference in ^{18}F-FP-CIT binding measured by PET/MR and PET/CT. The difference was mostly found in the caudate nucleus, and the voxelwise analysis revealed underestimated BR in periventricular areas in PET/MR, compared with PET/CT. To elucidate the difference, UTE-sequence-based attenuation maps were inspected, because non-AC images showed excellent interequipment agreement. We speculated that a misclassification of ventricles as air in UTE-based attenuation maps significantly caused underestimated BR in the caudate nucleus in PET/MR.

It is important to obtain accurate quantification in brain PET for clinical application considering development of quantitative image-based biomarkers and multicenter prospective trials. In particular, dopamine transporter imaging has been regarded as a biomarker for nigrostriatal dopaminergic dysfunction; thus, ^{18}F-FP-CIT binding was evaluated in several clinical trials (*25,26*). Of course, quantification of ^{18}F-FP-CIT binding has been a major issue in the clinical trials for a comparison between patients and serial follow-up for nigrostriatal degeneration. In this context, spatially and temporally coregistered MR combined with PET may have advantages in accurate definition of structures for quantification.

Though PET/MR has advantages in anatomic registration and brain tissue segmentation, it remains unclear whether brain PET/MR and PET/CT data are interchangeable. One of the most important problems was the inaccuracy of AC (*10*). Because Dixon sequence–based tissue segmentation to separate fat, soft tissue, and air is incorporated in dedicated PET/MR scanners, it has been regarded as a routine protocol in clinical whole-body PET/MR (*27*). However, it is difficult to differentiate bone from soft tissue using Dixon-based AC. Because the brain is surrounded by cortical bone, attenuation maps not accounting for bone necessarily lead to bias in quantification (*15*). UTE sequence–based bone segmentation has been regarded as an alternative to generate attenuation maps accounting for cortical bone. Despite taking account of bone attenuation, UTE-based attenuation maps had limitations in bony segmentation, resulting in incompleteness of bone tissue followed by underestimation of counts (*28*). Our data on UTE-based attenuation maps using PET/MR, compared with PET/CT, consistently demonstrated the incompleteness of cortical bone segmentation (Fig. 5). Moreover, we found that the thickness of cortical bone on UTE sequence–based AC maps in all cases was lower than on CT images on visual inspection, possibly also affecting AC. Nevertheless, attenuation maps accounting for cortical bones were regarded as better quantification for gray matter uptake than Dixon-based AC methods (*28*). As the difference map represented (Fig. 5), spatial quantification bias was more prominent in

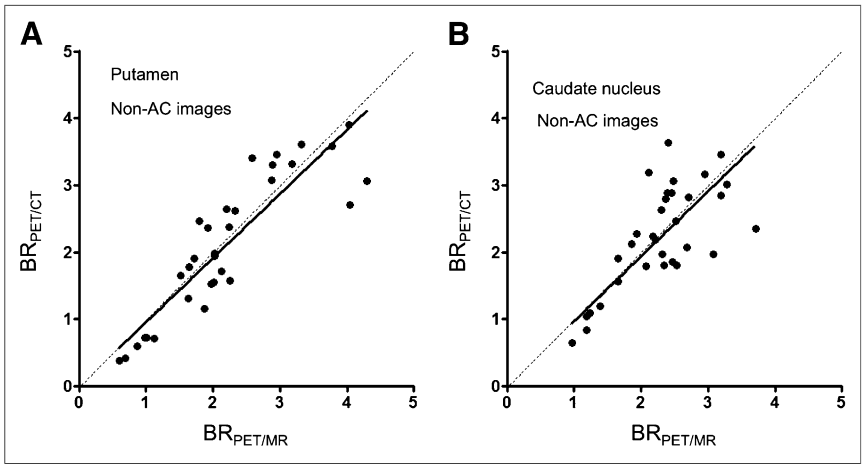

FIGURE 3. BR of PET/MR and PET/CT calculated from non-AC images. BR of putamen (A) and caudate nucleus (B) shows excellent interequipment agreement when non-AC images are applied (ICC, 0.937; 95% CI, 0.873–0.969, and ICC, 0.832; 95% CI, 0.655–0.918 for putamen and caudate nucleus, respectively).

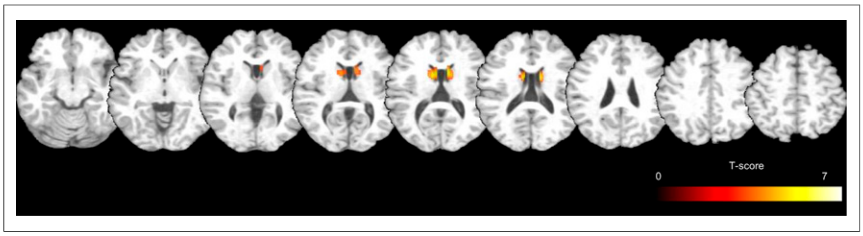

FIGURE 4. Voxelwise comparison between PET/MR and PET/CT. Image shows underestimated voxels in PET/MR using UTE sequence–based AC, compared with PET/CT (uncorrected $P < 0.001$ as a threshold with an extent threshold of 100 contagious voxels).

the periventricular area than in the cerebral neocortex, suggesting that cortical bone–related bias could be partly corrected by UTE sequence–based AC despite the incompleteness of bone segmentation.

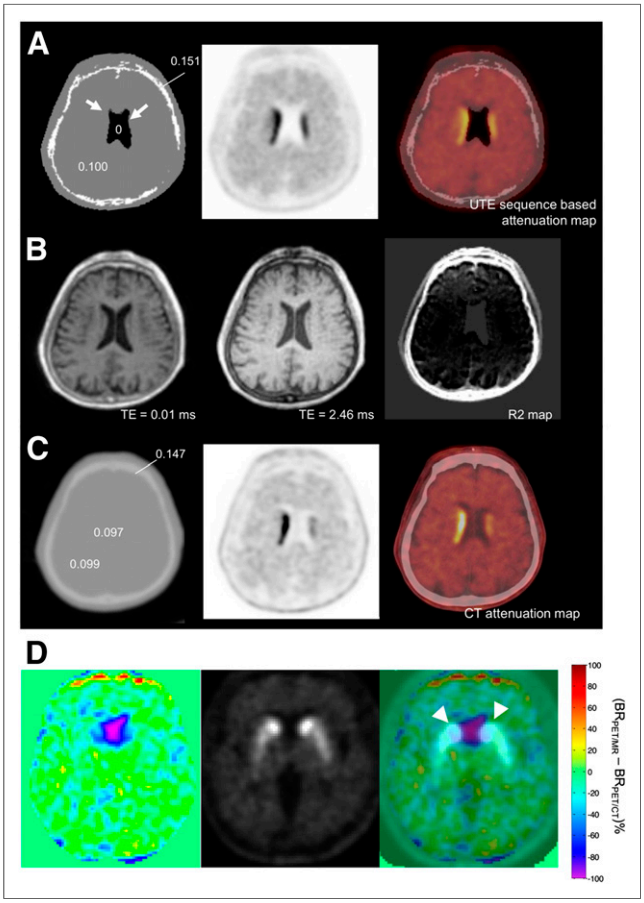

FIGURE 5. Representative images of UTE sequence–based AC and CT-based AC. (A) UTE sequence–based attenuation maps show misclassified voxels in lateral ventricle as air (arrow). (B) UTE images and R_2 maps for tissue classification. UTE images were acquired at echo times TE1 (0.07 ms)/TE2 (2.46 ms), and R_2 map is derived from 2 images after air mask. (C) CT-based attenuation map shows water attenuation in lateral ventricle. Difference in attenuation maps of PET/MR and PET/CT affects quantification of DAT BR. Numbers on attenuation map of PET/MR (A) and PET/CT (C) reveal attenuation coefficients of each region (cm^{-1}). Representative 1-cm-sized circular regions of interest were drawn on lateral ventricle, cortical bone, and brain tissue on CT-based attenuation map. (D) Difference image in percentage BR between PET images from PET/MR and PET/CT showed underestimation in lateral ventricles. Fusion images of difference map and ^{18}F-FP-CIT PET image showed that underestimation of BR was found in lateral ventricle, which overlapped caudate nucleus (arrowheads).

We showed spatial bias particularly in the caudate nucleus in ^{18}F-FP-CIT PET/MR, compared with PET/CT, though UTE sequence–based AC accounting for cortical bone was engaged. The spatial bias was caused by problems in differentiating soft tissue from air, which was different from previous reports with regard to ignoring bone attenuation. Though UTE sequence–based AC can separate bone, our results demonstrated additional problems in soft-tissue segmentation for generating optimal AC maps. Voxelwise analysis showed underestimated ^{18}F-FP-CIT BR in the periventricular area—that is, bilateral caudate nuclei. Previous studies revealed that UTE sequence–based AC had difficulties in determining the boundaries between air and soft tissue (*18,19*). For instance, bone tissues around paranasal sinuses were challenging when UTE sequence–based attenuation maps were applied (*29*). In our study, we found spatial bias in UTE sequence–based AC, which was a misclassification of cerebrospinal fluid space as air in attenuation maps. The findings were consistently observed in all patients despite the different extent of misclassification. Previous studies using UTE sequence–based segmentation also showed that a small fraction of the cerebrospinal fluid was misclassified as air (*17,19*).

Though MR-based AC has limitations, simultaneously acquired emission scans and MR data potentially have advantages in spatial registration during scan acquisition, compared with PET/CT scans. Thus, the optimal AC in PET/MR might provide accurate quantification with precise MR-based anatomic segmentation, though we used statistical probabilistic anatomic mapping rather than individual brain segmentation in this study. A new algorithm is required to obtain the accurate boundaries between air and soft tissue to solve the misclassification issue and eventually calculate reliable quantification.

We found excellent interchangeability (ICC for putamen was 0.937, and ICC for caudate nucleus was 0.832; ICC > 0.8 means statistically excellent interchangeability (*24*)) when non-AC data were applied. Furthermore, we visually inspected whether inaccurate AC maps directly distorted PET images from PET/MR and found that there was no significant difference between PET/CT and PET/MR. Those findings strongly suggest that differences in PET detectors have little effect on quantification. In our study, although we used PET/MR and PET/CT scanners from the same manufacturer, PET detectors were substantially different (*30*). Moreover, scan time and imaging protocols were not perfectly matched. Nevertheless, we obtained excellent ICC in non-AC data, implying that improved AC protocols in PET/MR promise accurate quantification equivalent to PET/CT.

In our results, other factors related to hardware components and reconstruction methods could affect the spatial bias of DAT BR. For the comparison of non-AC images, attenuation could be affected because the hardware components of the PET/MR scanner were different from those of the PET/CT scanner. In particular, non-AC images from PET/MR excluded attenuation of hardware components such as patient bridge or radiofrequency coils as well as patients' attenuation. Although the equipment has not been considered in the non-AC for PET/MR, it is unlikely that this exclusion resulted in the mitigation of underestimation of caudate nucleus activity shown in the attenuation-corrected data. The equipment would make a similar global impact on the putamen and caudate nucleus in terms of the AC factor because of the relatively long distance from these structures to the equipment. Both PET/MR and PET/CT used almost the same

reconstruction parameters as ordered-subset expectation maximization; however, the number of subsets was different (21 for PET/MR and 24 for PET/CT). We tested whether the number of subsets affected quantification of DAT BR, comparing PET images reconstructed by 12 and 24 subsets. The number of subsets had negligible effects on DAT BR quantification (the ICCs and 95% CIs were 0.999 and 0.998–1.000, respectively, for the putamen and 0.995 and 0.66–1.00, respectively, for the caudate nucleus) (Supplemental Fig. 1; supplemental materials are available at http://jnm.snmjournals.org).

The PET/MR study protocol, particularly UTE sequence–based AC, has recently been developed but not optimized. In the future, if the performance of UTE sequence–based tissue segmentation can be improved, accurate quantification of neuroreceptors or transporters will be achieved. One of the limitations of this study was serial PET protocols, PET/CT acquisition immediately after PET/MR. Thus, dynamic changes in ^{18}F-FP-CIT binding between the two scans were not fully considered. Although BR calculated from 90- to 120-min static images showed excellent correlation with binding potential (*20,21*), dynamic changes in ^{18}F-FP-CIT binding might partly result in the underestimation of striatal BR in PET/MR. Nevertheless, taking the non-AC PET data into consideration, we speculated that quantification bias in PET/MR was mainly affected by the AC method. Additionally, $BR_{caudate}$ fluctuated even when calculated by non-AC images, which could be related to more errors in quantification in the caudate nucleus than putamen due to small size. Despite the fluctuation, the underestimation of $BR_{caudate}$ on PET/MR was not found in non-AC images.

CONCLUSION

UTE sequence–based AC for ^{18}F-FP-CIT PET/MR caused spatial bias in quantification even though attenuation maps accounted for cortical bones. DAT BR was considerably underestimated in the caudate nucleus because of cerebrospinal fluid space misclassified as air in lateral ventricles. Because non-AC images showed remarkable interchangeability between PET/MR and PET/CT despite differences in PET detectors, a new algorithm for AC in PET/MR will improve quantification in brain PET.

DISCLOSURE

The costs of publication of this article were defrayed in part by the payment of page charges. Therefore, and solely to indicate this fact, this article is hereby marked "advertisement" in accordance with 18 USC section 1734. This study was supported by the Intramural Research Grant of Seoul National University and grant 0420130670 (2013-1290) from the SNU Research Fund. No other potential conflict of interest relevant to this article was reported.

ACKNOWLEDGMENTS

We thank Hyun-joon An and Yong Ho Do for their support during this study.

REFERENCES

1. Kinahan PE, Hasegawa BH, Beyer T. X-ray-based attenuation correction for positron emission tomography/computed tomography scanners. *Semin Nucl Med.* 2003;33:166–179.
2. Burger C, Goerres G, Schoenes S, Buck A, Lonn AH, Von Schulthess GK. PET attenuation coefficients from CT images: experimental evaluation of the transformation of CT into PET 511-keV attenuation coefficients. *Eur J Nucl Med Mol Imaging.* 2002;29:922–927.
3. Kazumata K, Dhawan V, Chaly T, et al. Dopamine transporter imaging with fluorine-18-FPCIT and PET. *J Nucl Med.* 1998;39:1521–1530.
4. Oh M, Kim JS, Kim JY, et al. Subregional patterns of preferential striatal dopamine transporter loss differ in Parkinson disease, progressive supranuclear palsy, and multiple-system atrophy. *J Nucl Med.* 2012;53:399–406.
5. Kim YI, Im HJ, Paeng JC, et al. Validation of simple quantification methods for ^{18}F-FP-CIT PET using automatic delineation of volumes of interest based on statistical probabilistic anatomical mapping and isocontour margin setting. *Nucl Med Mol Imaging.* 2012;46:254–260.
6. Kas A, Payoux P, Habert MO, et al. Validation of a standardized normalization template for statistical parametric mapping analysis of ^{123}I-FP-CIT images. *J Nucl Med.* 2007;48:1459–1467.
7. Jeong E, Oh SY, Pahk K, et al. Feasibility of PET template-based analysis on F-18 FP-CIT PET in patients with de novo Parkinson's disease. *Nucl Med Mol Imaging.* 2013;47:73–80.
8. Sipilä O, Nikkinen P, Pohjonen H, et al. Accuracy of a registration procedure for brain SPET and MRI: phantom and simulation studies. *Nucl Med Commun.* 1997;18:517–526.
9. Ciarmiello A, Giovacchini G, Guidotti C, et al. Weighted registration of ^{123}I-FP-CIT SPECT images improves accuracy of binding potential estimates in pathologically low striatal uptake. *J Cell Physiol.* 2013;228:2086–2094.
10. Hofmann M, Pichler B, Scholkopf B, Beyer T. Towards quantitative PET/MRI: a review of MR-based attenuation correction techniques. *Eur J Nucl Med Mol Imaging.* 2009;36(suppl 1):S93–S104.
11. Keereman V, Mollet P, Berker Y, Schulz V, Vandenberghe S. Challenges and current methods for attenuation correction in PET/MR. *MAGMA.* 2013;26:81–98.
12. Schulz V, Torres-Espallardo I, Renisch S, et al. Automatic, three-segment, MR-based attenuation correction for whole-body PET/MR data. *Eur J Nucl Med Mol Imaging.* 2011;38:138–152.
13. Martinez-Möller A, Nekolla SG. Attenuation correction for PET/MR: problems, novel approaches and practical solutions. *Z Med Phys.* 2012;22:299–310.
14. Keller SH, Holm S, Hansen AE, et al. Image artifacts from MR-based attenuation correction in clinical, whole-body PET/MRI. *MAGMA.* 2013;26:173–181.
15. Andersen FL, Ladefoged CN, Beyer T, et al. Combined PET/MR imaging in neurology: MR-based attenuation correction implies a strong spatial bias when ignoring bone. *Neuroimage.* 2014;84:206–216.
16. Kim JH, Lee JS, Song IC, Lee DS. Comparison of segmentation-based attenuation correction methods for PET/MRI: evaluation of bone and liver standardized uptake value with oncologic PET/CT data. *J Nucl Med.* 2012;53:1878–1882.
17. Catana C, van der Kouwe A, Benner T, et al. Toward implementing an MRI-based PET attenuation-correction method for neurologic studies on the MR-PET brain prototype. *J Nucl Med.* 2010;51:1431–1438.
18. Keereman V, Fierens Y, Broux T, De Deene Y, Lonneux M, Vandenberghe S. MRI-based attenuation correction for PET/MRI using ultrashort echo time sequences. *J Nucl Med.* 2010;51:812–818.
19. Aitken AP, Giese D, Tsoumpas C, et al. Improved UTE-based attenuation correction for cranial PET-MR using dynamic magnetic field monitoring. *Med Phys.* 2014;41:012302.
20. Scherfler C, Seppi K, Donnemiller E, et al. Voxel-wise analysis of [^{123}I]beta-CIT SPECT differentiates the Parkinson variant of multiple system atrophy from idiopathic Parkinson's disease. *Brain.* 2005;128:1605–1612.
21. Yaqub M, Boellaard R, van Berckel BN, et al. Quantification of dopamine transporter binding using [^{18}F]FP-beta-CIT and positron emission tomography. *J Cereb Blood Flow Metab.* 2007;27:1397–1406.
22. Lee JS, Lee DS. Analysis of functional brain images using population-based probabilistic atlas. *Curr Med Imaging Rev.* 2005;1:81–87.
23. Lee JS, Lee DS, Kim YK, et al. Probabilistic map of blood flow distribution in the brain from the internal carotid artery. *Neuroimage.* 2004;23:1422–1431.
24. Eliaszw M, Young SL, Woodbury MG, Fryday-Field K. Statistical methodology for the concurrent assessment of interrater and intrarater reliability: using goniometric measurements as an example. *Phys Ther.* 1994;74:777–788.
25. Iranzo A, Valldeoriola F, Lomena F, et al. Serial dopamine transporter imaging of nigrostriatal function in patients with idiopathic rapid-eye-movement sleep behaviour disorder: a prospective study. *Lancet Neurol.* 2011;10:797–805.
26. Schapira AH, McDermott MP, Barone P, et al. Pramipexole in patients with early Parkinson's disease (PROUD): a randomised delayed-start trial. *Lancet Neurol.* 2013;12:747–755.
27. Bezrukov I, Mantlik F, Schmidt H, Scholkopf B, Pichler BJ. MR-based PET attenuation correction for PET/MR imaging. *Semin Nucl Med.* 2013;43:45–59.
28. Dickson JC, O'Meara C, Barnes A. A comparison of CT- and MR-based attenuation correction in neurological PET. *Eur J Nucl Med Mol Imaging.* 2014;41:1176–1189.
29. Berker Y, Franke J, Salomon A, et al. MRI-based attenuation correction for hybrid PET/MRI systems: a 4-class tissue segmentation technique using a combined ultrashort-echo-time/Dixon MRI sequence. *J Nucl Med.* 2012;53:796–804.
30. Delso G, Furst S, Jakoby B, et al. Performance measurements of the Siemens mMR integrated whole-body PET/MR scanner. *J Nucl Med.* 2011;52:1914–1922.

JNM The Journal of NUCLEAR MEDICINE

Segmentation-Based MR Attenuation Correction Including Bones Also Affects Quantitation in Brain Studies: An Initial Result of ^{18}F-FP-CIT PET/MR for Patients with Parkinsonism

Hongyoon Choi, Gi Jeong Cheon, Han-Joon Kim, Seung Hong Choi, Jae Sung Lee, Yong-il Kim, Keon Wook Kang, June-Key Chung, E. Edmund Kim and Dong Soo Lee

J Nucl Med. 2014;55:1617-1622.
Published online: August 11, 2014.
Doi: 10.2967/jnumed.114.138636

The Journal of Nuclear Medicine is published monthly.
SNMMI | Society of Nuclear Medicine and Molecular Imaging
1850 Samuel Morse Drive, Reston, VA 20190.
(Print ISSN: 0161-5505, Online ISSN: 2159-662X)

SNMMI SOCIETY OF NUCLEAR MEDICINE AND MOLECULAR IMAGING